RSC Advances

PAPER

View Article Online
View Journal | View Issue

Cite this: *RSC Adv.*, 2019, **9**, 32338

A hierarchical $NiCo_2S_4$ honeycomb/$NiCo_2S_4$ nanosheet core–shell structure for supercapacitor applications

Lemu Girma Beka, Xin Li, Xiaoli Wang, Chuanyu Han and Weihua Liu *

Transition metal sulphides are becoming one of the promising materials for energy storage applications. Particularly, an advanced electrode material architecture, which gives favourable electronic and ionic conductivity, is highly in demand. Herein, a hierarchical $NiCo_2S_4$ honeycomb/$NiCo_2S_4$ nanosheet core–shell structure is reported for supercapacitor applications. The core–shell structure was *in situ* grown on a nickel foam *via* two consecutive hydrothermal processes, followed by an electrochemical deposition process. Moreover, we tuned the deposition cycle to get abundant active sites with gaps of suitable sizes between the walls of the honeycomb structure for efficient electrolyte diffusion routes. The 3D honeycomb core structure was used as superhighway for electron transport to the current collector, while the ultrathin shell structure offered a large surface area with short electron and ion diffusion paths, thus leading to the faster kinetics and higher utilization of active materials. Thus, using the synergistic advantages of the core material and the shell material, the as-synthesized optimized electrode material came up with an excellent specific capacitance of 17.56 F cm^{-2} at a current density of 5 mA cm^{-2} and the highest cycling stability of 88.2% after 5000 cycles of charge–discharge process. Such advanced electrode architectures are highly promising for the future electrode materials.

Received 28th July 2019
Accepted 19th September 2019

DOI: 10.1039/c9ra05840k

rsc.li/rsc-advances

1. Introduction

Energy storage devices are expected to be one of the most important devices in the coming era of internet of things and electric vehicles. Among the existing energy storage technologies, recently, supercapacitors are one that are growing rapidly because of their high power density,[1] resulting from their surface charge storing mechanism and long cycling stability.[2–4] However, supercapacitors have low energy density, which limits their practical applications.[5] Thus, it is important to rationally design electrode materials that can deliver high energy density without the compromise of good power density and cycle stability. In the past decade, supercapacitor technology has experienced an impressive performance improvement by using the concept of a nanostructured material design.[6–8] However, most of the reported electrode materials have their respective advantages and limitations to satisfy the challenging requirements in practical applications. Carbon-based materials exhibit excellent electrochemical aspects, such as conductivity and cycling stability, but suffer from low specific capacitance.[9,10] Transition metal-based materials deliver higher specific capacitance than carbon materials.[11] However, transition metal-based electrode materials suffer from poor rate capability and short cycling time.

Among transition metal-based electrode materials, nickel cobalt sulphides are one of the promising electrode materials for supercapacitor applications due to their low cost and natural abundance.[12–18] However, they suffer from poor capacity retention and short cycling stability. Their poor capacity retention is attributed to poor electrical conductivity and ion diffusion kinetics at higher current densities, while the short cycling stability is attributed to large volume changes during charge–discharge process, which lead to cracks.

So, the design of transition metal sulphide electrode materials with advanced architectures that leads to enlarged specific surface area, controlled porosity, and increased conductivity, which can result in fast electrode kinetics and long cycling stability, are highly in demand.[19–24] Thus, different architectures of transition metal sulphides are proposed to solve these issues, among which hierarchical core–shell structures are highly interesting architectures.[25–29] In such designs, the core structure can considerably enhance the electronic conductivity by using the direct path to the current collector, which increases the rate capability. However, the shell structure gives remarkable electrochemical active sites by direct access to the electrolyte. Particularly, three dimensional open structures with controlled core–shell structures, which can provide short diffusion paths for ions along the shell structure and facilitate electron transfer to the current collector along the core structure, are highly attractive.

School of Microelectronics, School of Electronic and Information Engineering, Xi'an Jiaotong University, Xi'an, 710049, P. R. China. E-mail: lwhua@mail.xjtu.edu.cn

In this study, we report a hierarchical NF/$NiCo_2S_4$ honeycomb/$NiCo_2S_4$ nanosheet core–shell structure (NF/NCS/NCS) for supercapacitor applications. The NCS core with the honeycomb 3D open structure could serve as an excellent scaffold to support NCS ultrathin and porous nanosheets and facilitate electron transport to the current collector. Moreover, the ultrathin nanosheets of NCS with multiple active sites were an interesting architecture for improving the specific capacitance of the as-synthesized active material. Moreover, we tuned the shell structures by changing the deposition cycle to get an optimized shell structure. Thus, the best core–shell material exhibited an excellent electrochemical performance of 17.56 F cm^{-2} at a current density of 5 mA cm^{-2}, which is by far better than materials without shell structures, with an electrochemical performance of 6.05 F cm^{-2} at a current density of 5 mA cm^{-2}. Moreover, the as-synthesized best electrode showed an excellent cycling stability of 88.2% after 5000 cycles of charge–discharge process, which is by far better than the materials without shell structures. Therefore, considering the excellent properties of the core structure to serve as a super electron pathway and the forest-like structure shell with abundant active sites, the as-synthesized electrode material is an excellent candidate for future energy storage applications.

2. Experimental

2.1 Material synthesis

In this experimental study, all the materials were used without any further processing and modifications. There were three key steps used to synthesize the NF/NCS/NCS core–shell structure. Step I: the synthesis of a honeycomb-like precursor on a nickel foam: in detail, 1.9 g of $NiCl_2 \cdot 6H_2O$, 1.9 g of $CoCl_2 \cdot 6H_2O$ and 0.72 g of urea were added into 50 ml of DI water and stirred until a homogeneous solution was obtained. A nickel foam (NF) of area 3 × 4 cm^2 was cleaned in ethanol using ultrasonication for 10 min, followed by cleaning using DI water. Then, the cleaned NF was diagonally placed in the solution and hydrothermally treated in an autoclave machine for 6 h at a temperature of 120 °C. Step II: sulfidation process, 2 g of $Na_2S \cdot 9H_2O$ was added to 50 ml of DI water and stirred to get a homogeneous solution, and the precursor sample prepared in step 1 was diagonally placed in the solution. Then, the sample was hydrothermally treated for 6 h at a temperature of 160 °C. After normally cooling down to room temperature, it was washed and dried and a NF/$NiCo_2S_4$ honeycomb scaffold structure was obtained. Step III: decorating the NF/$NiCo_2S_4$ honeycomb scaffold by a shell structure using an electrochemical deposition method. In detail, 0.1148 mg of $CS(NH_2)_2$, 0.02376 mg of $NiCl_2 \cdot 6H_2O$ and 0.11892 mg of $CoCl_2 \cdot 6H_2O$ were homogeneously dispersed into 100 ml of DI water. Then, three electrode configuration electrochemical workstation was used to deposit a shell structure using cyclic voltammetry at scan rate of 1 mV s^{-1}.

2.2 Structural characterization methods

Different structural characterization techniques, namely, field emission scanning electron microscopy (FE-SEM, Gemini SEM 500, Zeiss, Germany), field emission transmission electron microscopy (FE-TEM, JEOL JEM-F200 (HR)) and X-ray diffraction (XRD) (Bruker D8 ADVANCE), were used to study the structure of the as-synthesized materials at different experimental steps.

2.3 Electrochemical characterization methods

A three-electrode configuration electrochemical workstation was used to study the electrochemical properties of the as-synthesized material. In the three-electrode configuration the active material was used as the working electrode, while Hg/HgO and platinum sheet were used as the reference and counter electrodes, respectively. The working electrode was prepared using 1 × 1 cm^2 of the as-synthesized sample and pressing NF at 10 MPa to form a thin nickel foil. In all tests, 2 M KOH was used as an electrolyte. Then, electrochemical characteristic information were collected using cyclic voltammetry (CV), galvanic charge/discharge (GCD) and electrochemical impedance spectroscopy (EIS) tests.

The value of areal specific for all samples was calculated from the GCD plots, using the following eqn (1):[30,31]

$$C_A = \frac{I \times \Delta t}{A \times \Delta u} \quad (1)$$

where C_A (F cm^{-2}) is the areal specific capacitance, A (cm^2) is the area of the electrode material, I (A) is the discharge current, Δt (s) is the discharging time and Δu (V) is the operating potential window.

3. Results and discussion

3.1 Structural characterization

The synthesis process of the NF/NCS/NCS core–shell structure is schematically presented in Fig. 1. The first step is to synthesize a honeycomb precursor on the Ni foam substrate *via* a hydrothermal process (Fig. 1, step I). The second step is to transform a honeycomb-like precursor to a $NiCo_2S_4$ honeycomb structure using a sulphidation process.[32] The third step is the deposition of $NiCo_2S_4$ ultrathin nanosheets on the $NiCo_2S_4$ honeycomb to form a core–shell (NF/NCS/NCS) structure, as shown in Fig. 1, step III.

Fig. 2 shows typical SEM images of the NF/NCS honeycomb core structure and NF/NCS/NCS core–shell structures at different magnifications. As it can be clearly seen in Fig. 2a, free-standing and well-aligned NCS honeycomb are grown on the Ni foam substrate *via* a hydrothermal process. The walls of the honeycomb have a thickness of around 70 nm. In Fig. 2b and c, open free space can be clearly observed between the walls of the honeycomb structure, which is large enough to incorporate additional active materials in order to increase the specific capacitance of the device. Thus, we wrapped the walls of honeycomb with ultrathin nanosheets by a deposition process. Fascinatingly, we tuned the amount of the nanosheet-like shell on the walls by controlling the deposition cycle to balance electrolyte ions penetration into the active materials and the amount of active materials used as a shell. Thus, we prepared different samples by varying the deposition cycle numbers. The

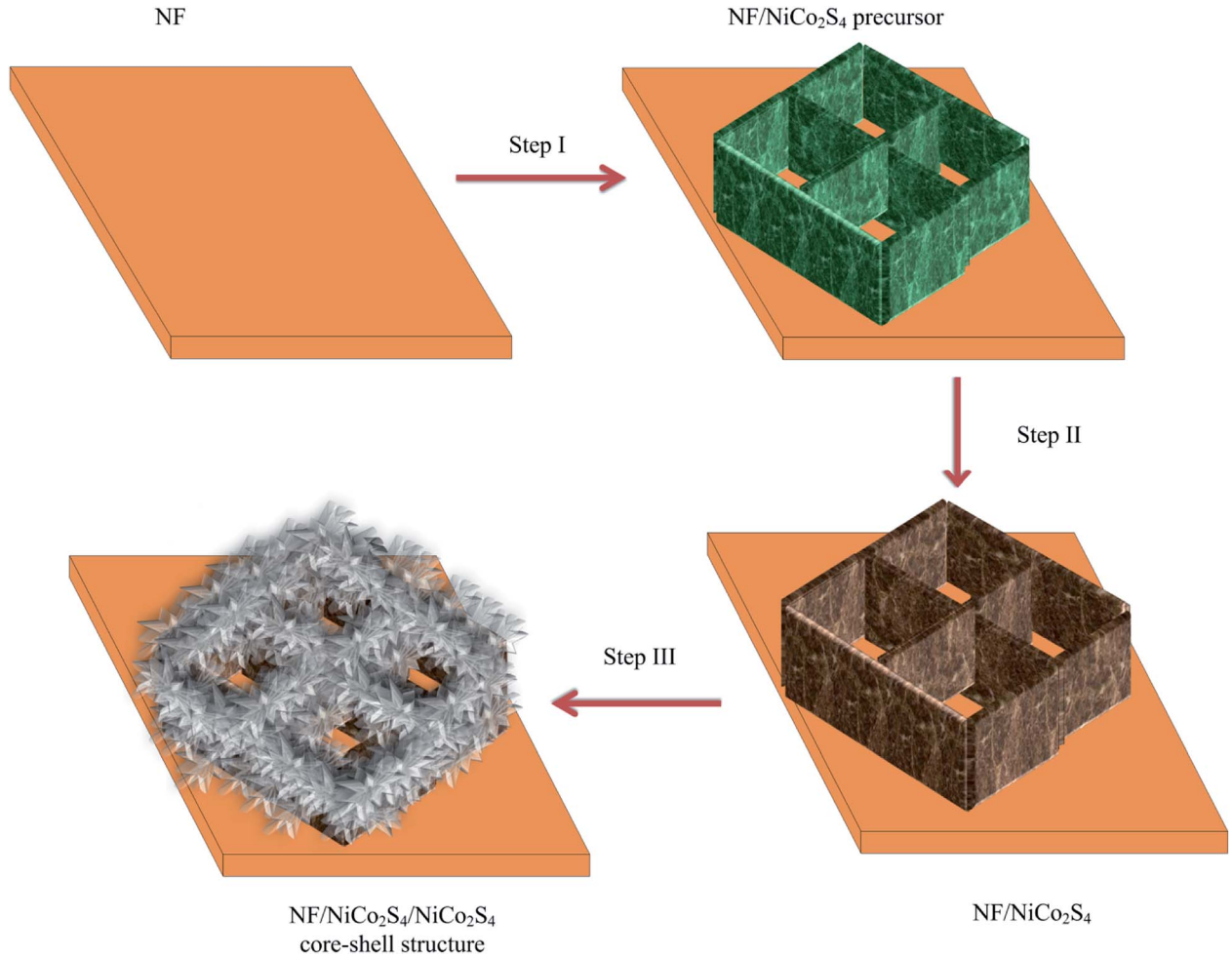

Fig. 1 Schematic of the experimental process.

samples are labelled as NF/NCS/NCS-0 sample prepared using 0 cycles of deposition (it is simply sample without shell (Fig. 2a–c)), NF/NCS/NCS-5 sample prepared using 5 cycles of deposition, NF/NCS/NCS-10 sample prepared using 10 cycles of deposition, NF/NCS/NCS-15 sample prepared using 15 cycles of deposition and NF/NCS/NCS-20 sample prepared using 20 cycles of deposition. Fig. 2d–f show the SEM image of NF/NCS/NCS-5. The SEM images clearly show that an ultrathin sheet shell material is grown on the walls of the NCS honeycomb structure. As the deposition cycles increased to 10 cycles (NF/NCS/NCS-10), the size of nanosheets covering the core structure proportionally increased. When the deposition cycle is further increased to 15 cycles (Fig. 2j–l), the free space between the walls is almost completely closed and the backbone core structure is completely covered by nanosheets. As the cycle number is increased to 20 cycles, the core structure is completely buried and the shell material with a forest-like structure with big trees is obtained (Fig. 2m–o). Thus, as the deposition cycle number is increased from 0 to 20 cycles, clear variation in the size of the shell structure is observed. In general, such a hierarchical 3D open structure directly grown on a current collector is highly desirable for supercapacitor applications.

For further understanding the structure of the as-synthesized material, we performed the TEM analysis. Fig. 3 shows typical FE-TEM and HRTEM images of NF/NCS/NCS-10. Fig. 3a and b clearly show that the surface of the wall (core structure) is wrapped with sheet-like structure, forming a typical core–shell structure. Fig. 3c shows the TEM images of the shell structure. Clearly, the TEM images show that ultrathin nanosheets are clearly grown on the surface of the core structure. Moreover, the high-resolution TEM (HRTEM) images are shown in Fig. 3d–f. Clearly, Fig. 3d shows a clear core–shell structure, where the core material is highly crystalline and the shell material is less crystalline compared to the core material. To confirm the crystal structure of the core–shell material, the magnified image of Fig. 3d is shown in Fig. 3e. The lattice fringes 2.8, 2.3, 1.8 and 1.6 nm can be indexed to the 311, 400, 511 and 440 crystal planes of $NiCo_2S_4$ (PDF #20-0782). It can be seen from Fig. 3d and e that the shell material is relatively in an amorphous phase compared to the core material; to confirm this, we have shown additional HRTEM images in Fig. 3f taken from the tip of Fig. 3c.

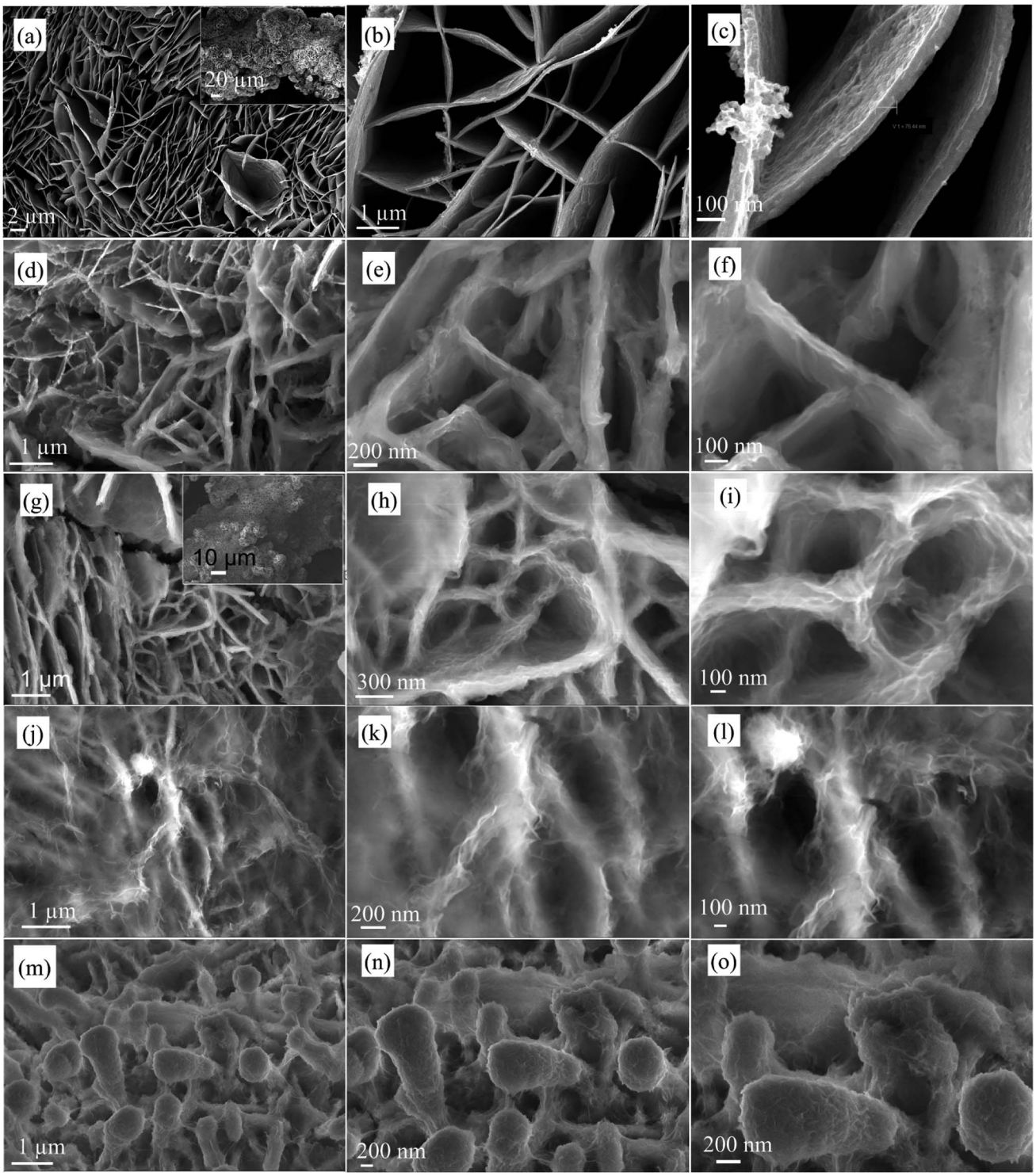

Fig. 2 FE-SEM images of NF/NCS/NCS at different deposition cycles (a–c) NF/NCS/NCS-0 at different magnifications, (d–f) NF/NCS/NCS-5 at different magnifications, (g–i) NF/NCS/NCS-10 at different magnifications, (j–l) NF/NCS/NCS-15 at different magnifications, (m–o) NF/NCS/NCS-20 at different magnifications.

To determine the elements in the as-synthesized material, we conducted EDS elemental mapping, and the result is displayed in Fig. 4. The elemental mapping images (Fig. 4b–d) indicate that the as-synthesized material is made of Co, Ni and S elements, respectively. To study the crystal structure of the as-synthesized hybrid material, we conducted XRD analysis before and after the formation of shell structure. Fig. 4e shows the XRD spectra of the as-synthesized materials before and after shell formation (sample NF/NCS/NCS-10). From the XRD peaks, the strong peaks at around 44.5 and 52 belong to the Ni foam

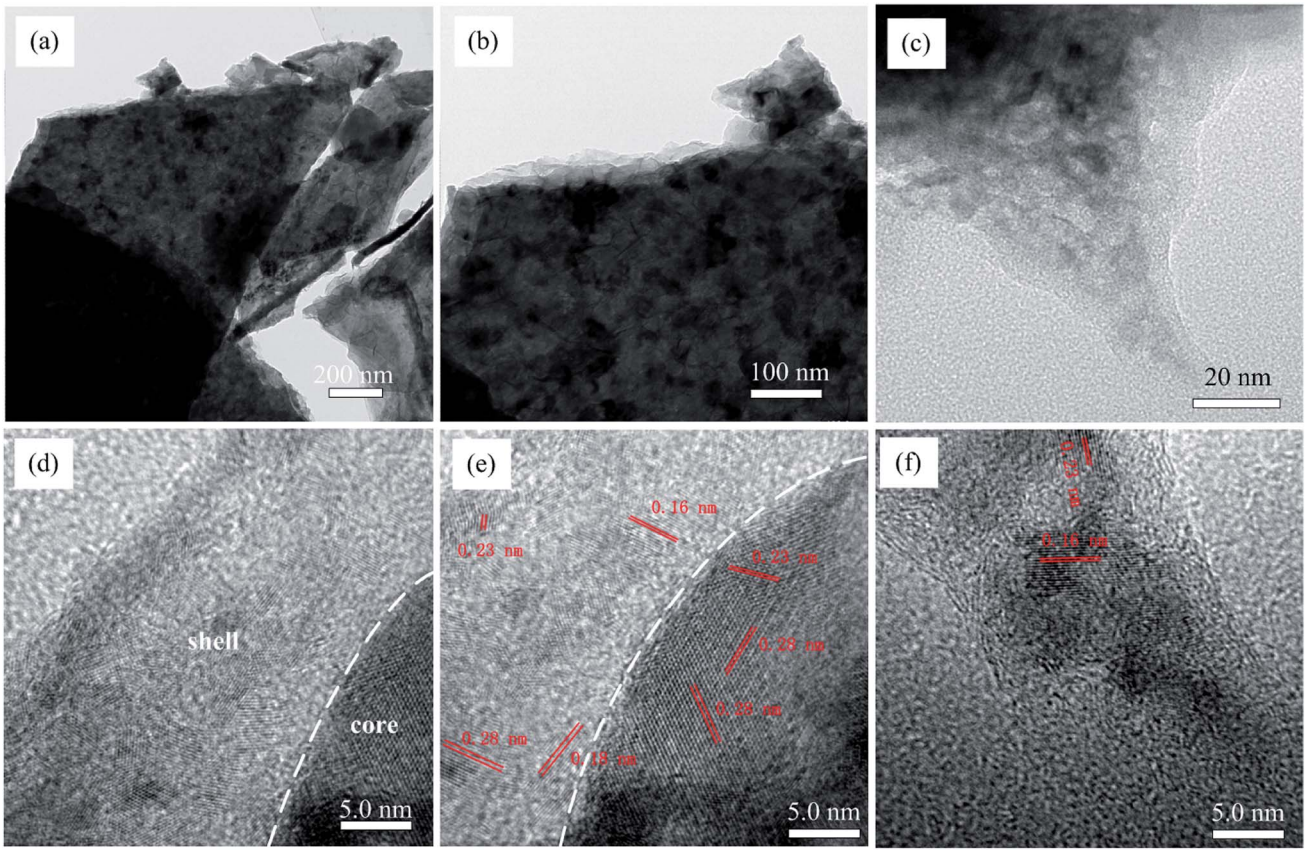

Fig. 3 (a–c) FE-TEM image of NF/NCS/NCS-10, (d) HRTEM image to illustrate the core/shell structure, (e) HRTEM image to illustrate the crystal structure of core and shell materials taken from (d) and (f) HRTEM image taken from tip of (c).

crystal plane for all samples. Fig. 4e$_1$ shows the XRD spectrum of the honeycomb pristine core material. It shows peaks at 26.867, 31.659, 38.55, 50.46 and 55.4°, which can be indexed to the 220, 311, 400, 511 and 440 crystal planes of $NiCo_2S_4$ (PDF #20-0782), respectively. The absence of other peaks clearly demonstrates that a pure crystal phase is prepared. Fig. 4e$_2$

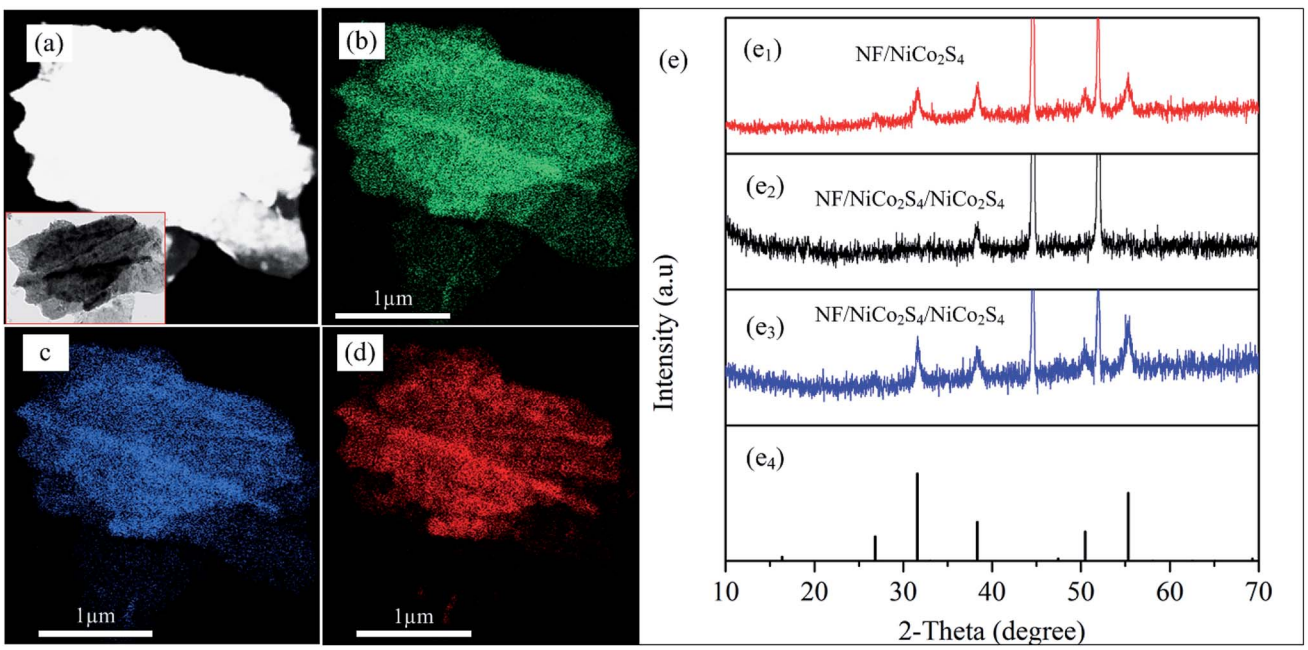

Fig. 4 (a) STEM image where EDS mapping taken, the inset is TEM image where EDS mapping taken, (b–d) EDS image of Co, Ni and S, respectively, (e) XRD spectra.

shows the XRD spectrum of a core/shell structure just after deposition and drying process. There are no clear peaks observed in this material except the NF peaks. This demonstrates that the core material was covered with abundant amorphous shell materials and showed weak crystal peaks. Thus, to increase the crystallinity of the sample, we annealed the core–shell material at a temperature of 100 °C for 1 h, and after annealing the crystal structure was clearly determined from the XRD spectrum as shown in Fig. 4e$_3$. Thus, the forest-like shell material has similar crystal structure to that of the original honeycomb material. Thus, the overall core–shell material is an $NiCo_2S_4$ honeycomb/$NiCo_2S_4$ forest-like sheet with a cubic crystal structure. Fig. 4e$_4$ shows the standard crystal peaks of $NiCo_2S_4$ with card number of (PDF #20-0782).

3.2 Electrochemical characterization

Fig. 5 shows a typical comparative electrochemical performance of NF/NCS/NCS-0, NF/NCS/NCS-5, NF/NCS/NCS-10, NF/NCS/NCS-15 and NF/NCS/NCS-20 samples. Fig. 5a shows comparative CV curves at a scan rate of 1 mV s^{-1}. All the samples showed clear redox active peaks, illustrating pseudocapacitive property. Clearly, Fig. 5a shows that all the samples with a core–shell structure illustrate better CV areas compared to the sample without shell. This is attributed to the extra active sites introduced by the nanosheet shell structures to participate in redox reactions. As the deposition cycle number increased from 0 to 10 cycles, the CV area increased; however, as it further increased to 15 and 20 cycles, the CV area became decreased and less than that of the 10 cycle depostion. Thus, sample NF/NCS/NCS-10 has relatively showed the largest CV area compared to all samples, illustrating its excellent electrochemical performance. This may be attributed to the suitable sizes of nanosheets between the gaps of the honeycomb wall structure for sufficient diffusion of the electrolyte ions through the whole material. To determine the contribution of the nickel foam current collector, we included the CV test result of pristine NF in the comparative CV test. Clearly, as it can be seen from the plot, the NF has negligible contribution to the specific capacitance of the as-synthesized material. Fig. 5b shows the relative GCD plots of different samples at a current density of 30 mA cm^{-2}. All the GCD plots show nonlinear graphs, illustrating a pseudocapacitive property, which is in agreement with the CV plots. Similar to the CV plots, the area covered by the GCD plots of sample without shell structure is less than all other samples, illustrating clear advantage of shell structures.

The areal specific capacitance of the as-synthesized materials is calculated using eqn (1). The maximum areal specific capacitance obtained is 6.05, 10.5, 17.56, 13.81 and 16.7 F cm^{-2} at a current density of 5 mA cm^{-2} for samples NF/NCS/NCS-0, NF/NCS/NCS-5, NF/NCS/NCS-10, NF/NCS/NCS-15 and NF/NCS/NCS-20, respectively. Clearly all samples have showed excellent specific capacitance. Samples with core–shell have shown much better capacitance performance compared to sample without shell. This is directly attributed to the introduction of abundant electroactive sites for faradaic reactions in the shell part. The difference in capacitance performance for samples prepared at different cycle numbers is attributed to the density of shell structures decorated on the walls. At lower cycle numbers, few active materials were grown as a shell and few active sites were obtained. Moreover, at higher deposition cycle numbers, the open space between the walls of the honeycomb core structure was totally blocked, which led to a decreased electrolyte penetration, thus leading to a lower utilization of the active material. Then, at high deposition cycles, the core–shell structure could not provide enough space for the intimate contact between electrode and electrolyte, leading to less material utilization and low capacitance performance. Thus, the relatively highest specific capacitance of NF/NCS/NCS-10 is due to the abundant shell nanosheets grown on the honeycomb core to provide large active sites with gaps of suitable sizes between the walls of core–shell for efficient electrolyte diffusion routes. The ultrathin shell structure offered a large surface area with short electron and ion diffusion paths, thus leading to faster kinetics and higher utilization of the active material and leads to better specific capacitance. To further understand the electrode performance at different current densities, comparative specific capacitance is plotted in Fig. 5c. Clearly, samples with a lower shell density showed better rate capability because of highly open structures, which facilitate the deep penetration of electrolyte during charge–discharge process. However, as the density of forest-like shell is increased, it takes time for ions to diffuse in and out, and rate capability become lower.

In pseudocapacitive material, cycling stability is the key issue. Fig. 5d shows the comparative cycling stability test results of NF/NCS/NCS-0, NF/NCS/NCS-5, NF/NCS/NCS-10, NF/NCS/NCS-15 and NF/NCS/NCS-20. After 5000 cycles of charge–discharge process at a constant current density of 25 mA cm^{-2}, the retained capacitance is 76%, 82%, 88.2%, 91% and 79% for NF/NCS/NCS-0, NF/NCS/NCS-5, NF/NCS/NCS-10, NF/NCS/NCS-15 and NF/NCS/NCS-20, respectively. Clearly, all materials have shown good cycling stability. Comparatively, sample NF/NCS/NCS-5 showed the best retention, while sample NF/NCS/NCS-10 showed the next highest cycling performance after 5000 cycles of charge–discharge process. The result indicates that the stability of the device enhanced after grafting the walls of NCS by ultrathin shells. This is due to the robust hierarchical structure that protects the collapse of the core structure and leads to electrochemical degradation in the following ways. (1) In core–shell structures, the nanosheet shell prevents the electrolyte from directly contacting the core structure and better structural stability is obtained, while in a pristine NF-NCS honeycomb, the core directly interacts with the electrolytes, resulting in swelling and fracture, which thus lead to less cycling stability. (2) The shell structures are ultrathin structures and less affected by stress and strain during charge–discharge process. The cycling capability difference between different core–shell structures can be attributed to the size and density of NCS decorated on an NCS core material under the following conditions. In low density shells, the stress between nanosheets is decreased and better cycling stability is observed, while for high density stacked nanosheets, the volume changes during charge and discharge processes leads to stress, resulting in less cycling stability. To obtain more information about the

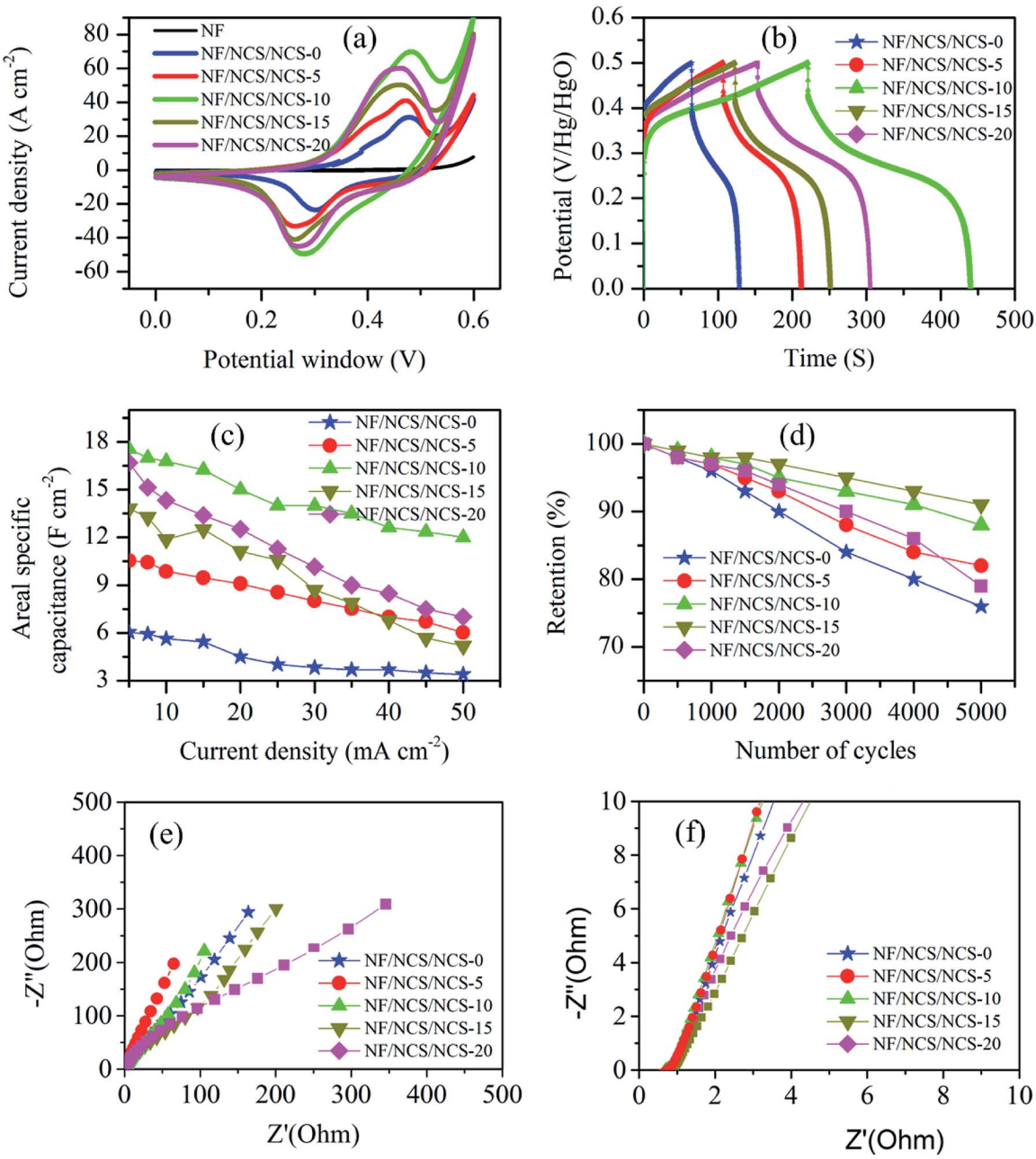

Fig. 5 Electrochemical performance test (a) relative CV plots at a scan rate of 1 mV s^{-1}, (b) relative GCD plots at a current density of 30 mA cm^{-2}, (c) relative areal specific capacitance as a function of current density, (d) cycling stability, (e) EIS plots at low frequency region and (f) EIS plots at high frequency region.

structural stability of our core/shell structure, we conducted SEM of the NF/NCS/NCS-10 active material after 5000 cycles of charge–discharge process. Even the SEM image (Fig. 6) shows a sheet-like structure warped on the core material, and a clear core/shell structure is obtained illustrating good structural stability of the as-synthesized active material after long cycling charge–discharge process. The cycling degradation observed after 5000 cycles of charge–discharge process may be due to the dropping of the active materials from nickel foam or the corrosion nickel foam after continuous charge–discharge process.

To understand the charge and ion transports in these materials, we conducted EIS test. Fig. 5e and f demonstrate the electrochemical impedance spectroscopy (EIS) test results of the as-synthesized materials. The EIS tests were conducted by applying a 5 V AC perturbation potential within the frequency range of 100 kHz to 0.1 Hz. It is well-known that the EIS plot has two key regions, namely, a high frequency region, which gives information about charge transfer rate,[33] and a low frequency region, which gives information about ion transportation in the active material.[34] Fig. 5e shows the low frequency relative EIS plots for NF/NCS/NCS-0, NF/NCS/NCS-5, NF/NCS/NCS-10, NF/

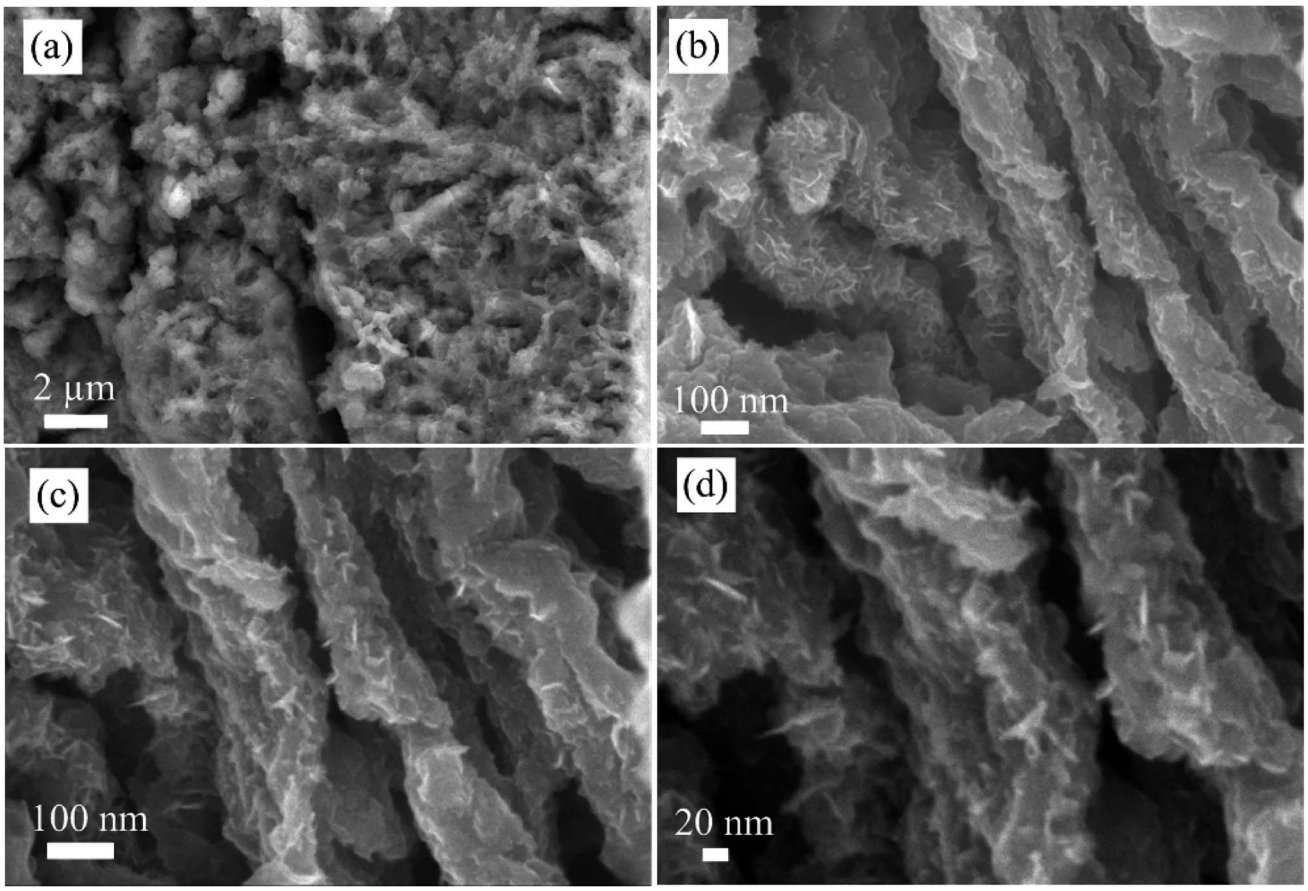

Fig. 6 SEM image of core/shell material after 5000 cycles of charge–discharge process at different magnification scales.

NCS/NCS-15 and NF/NCS/NCS-20. At low frequency region, NF/NCS/NCS-5 exhibits a more inclined line leaning to the imaginary axis, illustrating fast electrolyte ion transportation in the active material and more ideal capacitance behavior.[35] However, the highly loaded material NF/NCS/NCS-20 illustrates the least inclined line, illustrating less ion transportation compared to the other materials. This can be attributed to the blocking of the free space between the walls by the shell material and blocks deep penetration and diffusion of electrolyte ions. Materials with a more open structure facilitate easy transportation of electrolyte ions, while stacked/agglomerated structures show slow ion transportation. In the high frequency region (Fig. 5f), all the samples have shown almost negligible semicircle, illustrating excellent charge transport in all samples.

In summary, the excellent electrochemical performance of the NF/NCS/NCS core–shell electrode material could be attributed to the 3D hierarchical core–shell effects between NCS honeycomb core material and NCS forest-like ultrathin nanosheets in the following way. First, the honeycomb 3D open structure of the core structure served as an excellent open scaffold to load ultrathin nanosheets with favourable electron and ion transport along the material. Second, NCS honeycomb provides highly exposed active sites with accelerated ion diffusion and conductive skeleton, facilitating the electron transfer.

Table 1 Comparison of electrochemical performance of our NF/NCS/NCS with reported literature

Type of electrode	Specific capacitance	Cycling stability	Reference
$NiCo_2S_4$/Cobalt sulfide nanosheets	4.74 F cm^{-2}, 5 mA cm^{-2}	76.1%, 1500	36
$NiCo_2S_4$/Cobalt sulfide	714.2 mF cm^{-2}, 5 mA cm^{-2}	65%, 5000	37
Carbon close/$NiCo_2S_4$@$NiCo_2S$	245 mA h cm^{-2}, 2 mA cm^{-2}	86%, 3000	38
$NiCo_2S_4$@Ni_3S_2	4.25 C cm^{-2}, 4 mA cm^{-2}	—	39
CoS@$NiCo_2S_4$	7.62 F cm^{-2}, 5 mA cm^{-2}	71.7%, 3000	40
$NiCo_2S_4$/$Co_xNi_{(3-x)}S_2$	10.9 F cm^{-2}, 10 mA cm^{-2}	82%,5000	41
$NiCo_2S_4$/$Co(OH)_2$	9.6 F cm^{-2}, 2 mA cm^{-2}	70.01, 5000	42
$NiCo_2S_4$ honeycomb/$NiCo_2S_4$ nanosheet	17.56 F cm^{-2}, 5 mA cm^{-2}	88.2%, 5000	This study

Third, the nanosheets can afford more redox active sites and shortened ion diffusion pathways. Lastly, the *in situ* growth of the core–shell structure on the current collector can avoid additional conductive additives and polymer binders, thus providing high mechanical stability and conductivity. Using these advantages, the as-synthesized material has exhibited superior electrochemical performance compared with other reported literature listed in Table 1.

4. Conclusions

In summary, we successfully prepared a 3D hierarchical NF/NCS honeycomb decorated with NCS ultrathin forest-like nanosheets as a core–shell structure electrode material. The 3D hierarchical core–shell structure was grown by using a hydrothermal process, followed by sulfidation and electrochemical deposition processes. The optimized electrode material exhibited a high areal capacitance of 17.56 F cm^{-2} at a current density of 5 mA cm^{-2}, which is much better than the device without a shell structure (6.05 F cm^{-2} at the same current density). In addition, the as-synthesized material exhibited excellent rate capability and cycling stability compared with the material without the shell structure. The superior electrochemical performance essentially originated from the tuned core–shell structure with good electrical conductivity, and abundant electrochemical active sites originated from the core and shell structures. The proposed design strategy is straight forward to construct other 3D core–shell electrodes, which can be used in energy storage and conversion devices.

Conflicts of interest

The authors state as "There are no conflicts to declare".

Acknowledgements

The financial support of this work is by China Postdoctoral Science Foundation (Grant No. 2018M633511), the National Natural Science Foundation (Grant No. 61671368, 61172041, 91123018 and 61404103) and the Fundamental Research Funds for the Central Universities.

Notes and references

1 R. A. Huggins, *Solid State Ionics*, 2000, **134**, 179–195.
2 A. Burke, *J. Power Sources*, 2000, **91**, 2037–2050.
3 B. E. Conway, *Electrochemical supercapacitors: scientific fundamentals and technological applications*, Kluwer Academic/Plenum Publisher, New York, 1999.
4 M. Winter and R. J. Brodd, *Chem. Rev.*, 2004, **104**, 4245–4269.
5 G. Wang, L. Zhang and J. Zhang, *Chem. Soc. Rev.*, 2012, **41**, 797–828.
6 Y. Zhang, H. Feng, X. Wu, L. Wang, A. Zhang, T. Xia, H. Dong, X. Li and L. Zhang, *Int. J. Hydrogen Energy*, 2009, **34**, 4889–4899.
7 Z. S. Iro, *Int. J. Electrochem. Sci.*, 2016, 10628–10643.
8 G. Wang, L. Zhang and J. Zhang, *Chem. Soc. Rev.*, 2012, **41**, 797–828.
9 M. F. El-Kady, Y. Shao and R. B. Kaner, *Nat. Rev. Mater.*, 2016, **1**, 16033.
10 W. Lv, Z. Li, Y. Deng, Q.-H. Yang and F. Kang, *Energy Storage Materials*, 2016, **2**, 107–138.
11 J. Jiang, Y. Li, J. Liu, X. Huang, C. Yuan and X. W. Lou, *Adv. Mater.*, 2012, **24**, 5166–5180.
12 H. Chen, J. Jiang, L. Zhang, H. Wan, T. Qi and D. Xia, *Nanoscale*, 2013, **5**, 8879–8883.
13 W. Kong, C. Lu, W. Zhang, J. Pu and Z. Wang, *J. Mater. Chem. A*, 2015, **3**, 12452–12460.
14 B. Li, M. Zheng, H. Xue and H. Pang, *Inorg. Chem. Front.*, 2016, **3**, 175–202.
15 C. Xia, P. Li, A. N. Gandi, U. Schwingenschlögl and H. N. Alshareef, *Chem. Mater.*, 2015, **27**, 6482–6485.
16 H. Wan, J. Jiang, J. Yu, K. Xu, L. Miao, L. Zhang, H. Chen and Y. Ruan, *CrystEngComm*, 2013, **15**, 7649.
17 L. Shen, L. Yu, H. B. Wu, X. Y. Yu, X. Zhang and X. W. Lou, *Nat. Commun.*, 2015, **6**, 6694.
18 X. Wang, X. Xia, L. G. Beka, W. Liu and X. Li, *RSC Adv.*, 2016, **6**, 9446–9452.
19 Z. Yu, L. Tetard, L. Zhai and J. Thomas, *Energy Environ. Sci.*, 2015, **8**, 702–730.
20 A. S. Aricò, P. Bruce, B. Scrosati, J.-M. Tarascon and W. V. Schalkwijk, *Nat. Mater.*, 2005, **4**, 366–377.
21 L. G. Beka, X. Li, X. Xia and W. Liu, *Diamond Relat. Mater.*, 2017, **73**, 169–176.
22 L. G. Beka, X. Li, X. Xia and W. Liu, *Diamond Relat. Mater.*, 2017, **73**, 80–86.
23 C. Guan, X. Liu, A. M. Elshahawy, H. Zhang, H. Wu, S. J. Pennycook and J. Wang, *Nanoscale Horiz.*, 2017, **2**, 342–348.
24 A. M. Elshahawy, X. Li, H. Zhang, Y. Hu, K. H. Ho, C. Guan and J. Wang, *J. Mater. Chem. A*, 2017, **5**, 7494–7506.
25 N. T. Trang, H. V. Ngoc, N. Lingappan and D. J. Kang, *Nanoscale*, 2014, **6**, 2434–2439.
26 P. Yang, X. Xiao, Y. Li, Y. Ding, P. Qiang, X. Tan, W. Mai, Z. Lin, W. Wu, T. Li, H. Jin, P. Liu, J. Zhou, C. P. Wong and Z. LinWang, *ACS Nano*, 2013, **7**, 617–2626.
27 J. Liu, C. Cheng, W. Zhou, H. Li and H. J. Fan, *Chem. Commun.*, 2011, **47**, 3436–3438.
28 J. Wang, X. Zhang, Q. Wei, H. Lv, Y. Tian, Z. Tong, X. Liu, J. Hao, H. Qu, J. Zhao, Y. Li and L. Mai, *Nano Energy*, 2016, **19**, 222–233.
29 X.-w. Dong, Y.-y. Zhang, W.-J. Wang and R. Zhao, *J. Alloys Compd.*, 2017, **729**, 716–723.
30 D. Yu, K. Goh, H. Wang, L. Wei, W. Jiang, Q. Zhang, L. Dai and Y. Chen, *Nat. Nanotechnol.*, 2014, **9**, 555–562.
31 L. Huang, D. Chen, Y. Ding, S. Feng, Z. L. Wang and M. Liu, *Nano Lett.*, 2013, **13**, 3135–3139.
32 Y. Yin, C. K. Erdonmez, S. H. Andreu Cabot and A. P. Alivisatos, *Adv. Funct. Mater.*, 2006, **16**, 1389–1399.
33 R. Kötz and M. Carlen, *Electrochim. Acta*, 1999, **45**, 2483–2498.
34 J. R. Miller, R. A. Outlaw and B. C. Holloway, *Science*, 2010, **329**, 1637–1639.

35 M. D. Stoller, S. Park, J. A. Yanwu Zhu and R. S. Ruoff, *Nano Lett.*, 2008, **8**, 3498–3502.
36 W. Fu, C. Zhao, W. Han, Y. Liu, H. Zhao, Y. Ma and E. Xie, *J. Mater. Chem. A*, 2015, **3**, 10492–10497.
37 J.-W. Cheng, L.-Y. Lin, W.-L. Hong, L.-Y. Lin, H.-Q. Chen and H.-X. Lai, *Electrochim. Acta*, 2018, **283**, 1245–1252.
38 J. Xie, Y. Yang, G. Li, H. Xia, P. Wang, P. Sun, X. Li, H. Cai and J. Xiong, *RSC Adv.*, 2019, **9**, 3041–3049.
39 T. He, S. Wang, F. Lu, M. Zhang, X. Zhang and L. Xu, *RSC Adv.*, 2016, **6**, 97352–97362.
40 W. Zeng, G. Zhang, X. Wu, K. Zhang, H. Zhang, S. Hou, C. Li, T. Wang and H. Duan, *J. Mater. Chem. A*, 2015, **3**, 24033–24040.
41 L. G. Beka, X. Li and W. Liu, *Sci. Rep.*, 2017, **7**, 2105.
42 R. Li, S. Wang, Z. Huang, F. Lu and T. He, *J. Power Sources*, 2016, **312**, 156–164.